

# Inducing tensile failure of claystone through thermal pressurization in a novel triaxial device

Philipp Braun · Pierre Delage · Siavash Ghabezloo ·  
Baptiste Chabot · Nathalie Conil · Minh-Ngoc Vu

Accepted manuscript DOI: 10.1007/s00603-022-02838-3

## Highlights

- Thermal pressurization of clay rock in deep radioactive waste repositories can reduce the effective stresses, which can lead to damage or failure.
- Our novel laboratory triaxial device is able to mimic in situ conditions: Constant vertical total stress, zero lateral deformation and thermal pressurization.
- Pore pressure increase, vertical extension strains and thermal pressurization failure were recorded in a series of tests on Callovo-Oxfordian claystone specimens.
- The effective tensile strength was reached at values around 3 MPa in tension and temperatures between 53 and 64 °C, creating sub-horizontal fractures.
- The experimental responses can be well reproduced using a thermo-poroelasticity model.
- Hoek-Brown and Fairhurst generalized Griffith criteria appear suitable to account for the rock's tensile resistance.

---

P. Braun · S. Ghabezloo · P. Delage · B. Chabot ·  
Laboratoire Navier, 6-8 avenue Blaise-Pascal, Cité Descartes 77455 Champs-sur-Marne, Paris, France  
E-mail: philipp.braun@enpc.fr

P. Braun · M.-N. Vu  
Andra, 1 Rue Jean Monnet, 92290 Châtenay-Malabry, France

N. Conil  
Andra, Centre de Meuse/Haute-Marne BP9, 55290 Bure, France  
Now at: INERIS, Ecole des Mines, Parc de Saurupt, 54042 Nancy, France

**Abstract** Complex coupled thermo-hydromechanical (THM) loading paths are expected to occur in clay rocks which serve as host formations for geological radioactive waste repositories. Exothermic waste packages heat the rock, causing thermal strains and temperature induced pore pressure build-up. The drifts are designed in such a way as to limit these effects. One has to anticipate failure and fracturing of the material, should pore pressures exceed the tensile resistance of the rock. To characterise the behaviour of the Callovo-Oxfordian claystone (COx) under effective tension and to quantify the tensile failure criterion, a laboratory program is carried out in this work. THM loading paths which correspond to the expected in situ conditions are recreated in the laboratory. To this end, a special triaxial system was developed, which allows the independent control of radial and axial stresses, as well as of pore pressure and temperature of rock specimens. More importantly, the device allows one to maintain axial effective tension on a specimen. Saturated cylindrical claystone specimens were tested in undrained conditions under constrained lateral deformation and under nearly constant axial stress. The specimens were heated until the induced pore pressures created effective tensile stresses and ultimately fractured the material. The failure happened at average axial effective tensile stresses around 3.0 MPa. Fracturing under different lateral total stresses allows one to describe the failure with a Hoek-Brown or Fairhurst's generalized Griffith criterion. Measured axial extension strains are analysed based on a transversely isotropic thermo-poroelastic constitutive model, which is able to satisfactorily reproduce the observed behaviour.

**Keywords** Thermal pressurization · Tensile failure · Thermo-poroelasticity · Transverse isotropy · Callovo-Oxfordian claystone · Nuclear waste disposal

## List of Symbols

Note that the matrix notation is used throughout this work.

$h$	Direction parallel to bedding
$z$	Direction perpendicular to bedding
$\sigma_i$	Total stress in direction $i$
$\sigma'_i$	Terzaghi effective stress in direction $i$
$\varepsilon_i$	Strain in direction $i$
$\sigma_c$	Unconfined compressive strength
$\sigma_t$	Tensile strength
$E_i$	Young's modulus in direction $i$
$\nu_i$	Poisson's ratio in direction $i$
$m_i$	Hoek-Brown criterion parameter
$\phi$	Porosity
$\rho$	Wet density
$\rho_d$	Dry density
$w$	Water content
$S_r$	Degree of saturation
$s$	Suction
$p_f$	Pore pressure
$T$	Temperature
$\sigma$	Isotropic confining pressure
$\varepsilon_{hyd}$	Volumetric hydration swelling
$\gamma_t$	Fracture angle with respect to bedding
$C_{ij}$	Elastic compliance matrix
$b_i$	Biot's coefficient in direction $i$
$\alpha_{d,i}$	Drained thermal expansion coefficient in direction $i$
$G'$	Shear modulus within the isotropic plane
$G$	Shear modulus perpendicular to the isotropic plane
$\alpha_\phi$	Bulk thermal expansion coefficient of the pore volume
$M$	Biot's modulus
$K_f$	Bulk modulus of the pore fluid
$K_\phi$	Bulk modulus of the pore volume
$\varphi$	Friction angle
$c$	Cohesion
$V_L$	Volume of the drainage system
$c_L$	Compressibility of the drainage system with respect to fluid pressure
$p_L$	Fluid pressure within the drainage system
$\kappa_L$	Compressibility of the drainage system with respect to radial confining pressure
$\sigma_{rad}$	Radial confining pressure
$\alpha_L$	Bulk thermal expansion coefficient of the drainage system
$M_s$	Fluid mass within the specimen
$m_f$	Fluid mass per unit volume of the specimen
$V_s$	Total specimen volume
$M_L$	Fluid mass within the drainage system
$\rho_L$	Fluid density within the drainage system
$\rho_f$	Pore fluid density
$c_f$	Pore fluid compressibility
$\alpha_f$	Pore fluid bulk thermal expansion coefficient

## 1 Introduction

A detailed investigation of the thermo-poroelastic properties of host rocks is essential in the design of the deep geological disposals of high-level radioactive wastes in clay rocks, as considered in France, Switzerland and Belgium. Next to the hydro-mechanical response involved during the excavation of the micro-tunnels, a thermo-hydro-mechanical response takes place during to the heat release from the exothermic waste packages (e.g. Gens et al., 2007; Seyedi et al., 2017; Armand et al., 2017; Conil et al., 2020, see Fig. 1). Heat radiates from the packages, resulting in gradually increasing temperature in the rock. This so-called thermal pressurization occurs when saturated soils or rocks are heated in undrained conditions, due to the significant difference between the thermal expansion coefficients of water and of the solid phase (Ghabezloo and Sulem, 2009; Vu et al., 2020). Quasi-undrained conditions are provided through the very low permeability of the claystone (in the order of  $10^{-20}$  m<sup>2</sup>, Escoffier et al., 2005; Davy et al., 2007; Menaceur et al., 2015, 2016).

Thermal pressurization has been observed in various in situ heating tests carried out in underground research laboratories (URL) excavated in claystones. It has been described and numerically modelled by different authors (e.g. by Gens et al., 2007; Jobmann and Polster, 2007 in the HE-D test run in the Opalinus clay in the Mt Terri URL in Switzerland, by Seyedi et al., 2017; Conil et al., 2020 in the TED test and by Armand et al. (2017); Bumbieler et al. (2021); Tourchi et al. (2021) in the ALC1604 test, both run in the Callovo-Oxfordian claystone (COx) in the Bure URL in France). Thermal pressurization has also been investigated through laboratory experiments, as done by Mohajerani et al., 2012; Zhang et al., 2017; Braun et al., 2021a on COx claystone and Monfared et al., 2011b on Opalinus clay.

The thermo-poromechanical strain response of claystones in drained and undrained conditions has been investigated in the laboratory by various authors including Zhang et al., 2017; Mohajerani et al., 2014; Menaceur et al., 2016; Belmokhtar et al., 2017b,a; Braun et al., 2020, 2021a on the COx claystone and Monfared et al., 2011b and Favero et al., 2016 on the Opalinus clay. A thermo-elastoplastic behaviour upon drained heating under constant effective stress has been evidenced by Monfared et al., 2011b on the Opalinus clay and by Belmokhtar et al., 2017a; Braun et al., 2020, 2021a on the COx claystone. The latter authors found that both elastic and plastic drained strains were anisotropic during the tests. These features are somewhat similar to what has been observed in previous investigations on clays (e.g. Baldi et al., 1988; Sultan et al., 2002 on Boom clay and Abuel-Naga et al., 2007 on Bangkok clay).

Figure 1a illustrates schematically the current French concept for high level radioactive waste disposal at great depth, in which waste canisters are deposited in parallel horizontal sleeved micro-tunnels of 0.7 to 1.0 m diameter and 80 to 150 m length (Armand et al., 2015; Plúa et al., 2021a,b). The micro-tunnels are evenly spaced with enough distance such as to keep the temperature below 90 °C in the rock and to ensure no damage in the far field. Given the length of the micro-tunnels and their periodic layout, thermo-hydro-mechanical processes are often modelled assuming plane strain conditions (Fig. 1b), with symmetry conditions at mid-distance between them. This results in peculiar conditions at this location, i.e. zero horizontal deformations and no horizontal heat nor fluid flux. One can expect a significant thermal pore pressure build-up in this area, since the horizontal fluid flow is limited through the no-flux boundary conditions. With time, thermal pore pressures dissipate towards the far-field. In summary, the rock mass at this mid-distance is submitted to zero lateral deformation, constant overburden vertical total stress and temperature increase. Constrained lateral thermal expansion leads to an increase of lateral total stress. In such conditions, one has to consider the risk of reaching a pore pressure level larger than the total vertical stress, which could lead to local vertical tensile failure (Li and Wong, 2018). Note that the planned design of the high level radioactive waste repository does not allow any tensile failure. More importantly, the study of thermally induced fracturing is crucial for risk management.

The tensile strength of clay-rocks has been widely investigated in rock mechanics, and commonly measured through the direct tension test (Hoek, 1964; Brace, 1964) or the Brazilian test (Akazawa, 1943; Carneiro, 1943; ISRM, 1978). Yang and Hsieh (1997) determined the tensile strength of a transversely isotropic claystone in direct tension tests. They evidenced a smaller tensile resistance for tension applied perpendicular to the plane

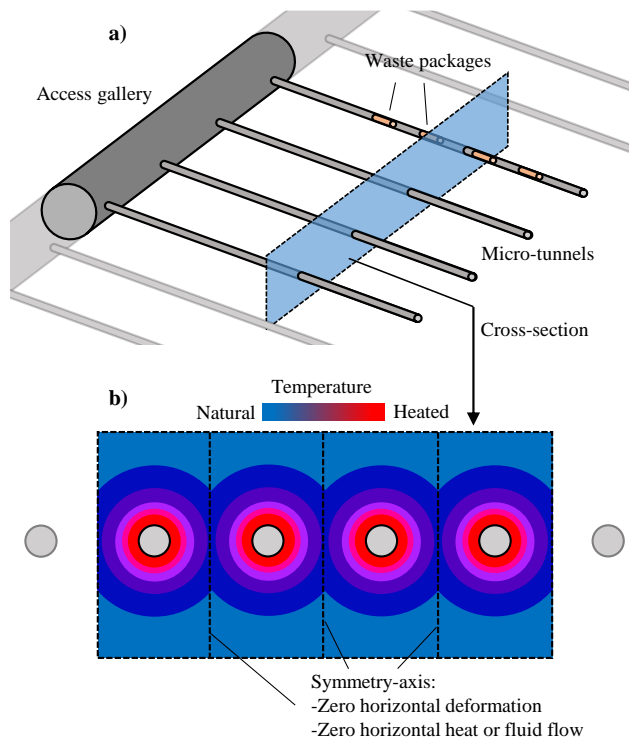


**Fig. 1** a) Layout of the micro-tunnels containing high-level radioactive waste (adopted from Andra, 2005), with b) a cross-section where one can assume plane strain and zero heat and temperature flux perpendicular to the image plane, illustrating the heat radiation from periodically constructed micro-tunnels.

of isotropy ( $\sim 4$  MPa) with respect to that measured on specimens loaded parallel to the plane of isotropy ( $\sim 11.5$  MPa). Interestingly, under tension loading, they found elastic material properties close to the values measured under compression. Only the Young modulus perpendicular to the plane of isotropy was detected to be higher in tension than in compression. They observed a quite linear stress-strain behaviour under tension. Coviello et al. (2005) carried out various different types of tensile tests, to determine the strength of two types of weak rocks, Gasbeton and calcarenite. In the case of calcarenite, they found the same tensile strength with both direct tensile test and Brazilian test ( $\sim 0.6$  MPa). In the case of Gasbeton, the strength measured with direct tension ( $\sim 0.9$  MPa) was higher than measured in Brazilian tests ( $\sim 0.5$  MPa). They noted that for both materials, the Young moduli in tension and compression were about the same, with a very linear stress-strain behaviour until failure. In the work of Hansen and Vogt (1987), an overview of various shales and claystones is given with their unconfined compressive strength, elastic properties and tensile strength, presented in Tab. 1. These are compared with the data from Bossart (2011) on the Opalinus clay.

According to Diederichs (2007), one can estimate  $\sigma_t = \sigma_c/m_i$ , where  $\sigma_t$  is the tensile strength,  $\sigma_c$  the unconfined compressive strength and  $m_i$  a material constant of the Hoek-Brown model. An estimation for claystone of  $m_i \approx 4.0 \pm 2$  is recommended by Hoek (2007). Even though Perras and Diederichs (2014) concluded that this formula does not give accurate results, it can be used to get a first approximation of the tensile resistance of brittle rocks. The calculated values for  $m_i$  of some shales and claystones are presented in Tab. 1, confirming that they are generally higher than the recommended value of  $4.0 \pm 2$ . One observes a rather large

**Table 1** Shale and claystone characteristics adopted from the literature, with an estimation of the Hoek-Brown coefficient  $m_i = \sigma_c/\sigma_t$ , compared with the experimental results of this study on COx claystone

Rock type	$\sigma_c$ [MPa]	$E$ [GPa]	$\nu$ [-]	$\sigma_t$ [MPa]	$m_i$ [-]
Pierre shale <sup>1</sup>	7.2	0.6	0.12	0.5	13.6
Rhinestreet shale <sup>1</sup>	58.7	17.5	0.19	8.4	7.0
Green river shale <sup>1</sup>	94.8	10.4	0.31	11.9	8.0
Carlile shale <sup>1</sup>	22.8	3.3	0.16	3.5	6.5
Colorado shale <sup>2</sup>	2.97	2.4	0.42	0.4	6.9
Opalinus clay $\perp$ <sup>3</sup>	25.6	2.8	0.33	2.0	12.8
Opalinus clay $\parallel$ <sup>3</sup>	10.5	7.2	0.24	1.0	10.5
COx claystone $\parallel$	17.8 <sup>4</sup>	5.7 <sup>5</sup>	0.29 <sup>5</sup>	3.0 <sup>6</sup>	5.15 <sup>6</sup>

<sup>1</sup>Hansen and Vogt (1987),

<sup>2</sup>Mohamadi and Wan (2016), <sup>3</sup>Bossart (2011),

<sup>4</sup>Andra database, <sup>5</sup>Braun et al. (2021b), <sup>6</sup>this study

variability of  $m_i$  for these clay rocks between 6.5 and 13.6. Among the aforementioned studies, authors did not investigate a temperature dependency of the tensile resistance.

The possibility of fracturing claystones through temperature-induced pore pressures has been recently demonstrated by Li and Wong (2018) through laboratory unconfined heating tests. In lack of any stress and strain measurements, these authors supposed that the fractures, that propagated parallel to the bedding plane, were induced when the pore pressure exceeded the tensile strength. To the authors best knowledge, the thermal fracturing of geomaterials has hitherto not been investigated under laboratory conditions of controlled stresses, pore pressure and temperature. This paper presents the development of a novel thermal extension triaxial device aimed at mimicking the thermal extension failure phenomenon under particular stress paths. The test results show the THM response of the COx claystone from the intact to the fractured state when subjecting it to thermal pressurization and provide an appropriate criterion accounting for its thermally induced tensile failure.

## 2 Novel experimental device

This work's aim was to develop a thermal extension triaxial device, in which a specimen should be submitted in undrained conditions to a temperature increase. At the same time, radial strain has to remain zero and vertical total stress constant, which corresponds to the in situ overburden stress. The zero radial stress condition involves a servo-control of the confining pressure, while maintaining pore pressures larger than the total vertical stress is another experimental challenge.

Similar to previous thermal testing devices developed and used in the same research group at Ecole des Ponts ParisTech (e.g. Menaceur et al., 2016; Belmokhtar et al., 2017a; Braun et al., 2021a), a triaxial cell (Fig. 2a) was employed for the laboratory tests. A pressure volume controller (PVC1, GDS brand) was used to apply pressure to the axial piston and to control the axial stress. Additional PVCs (PVC2,3, GDS brand) were used to control the confining pressure and the pore pressure separately. Temperature changes were applied by using an electric silicone heating belt, wrapped around the steel cell, and measured by means of a thermocouple located inside the cell. Local (radial and axial) strains were accurately monitored by means of strain gages glued directly onto the sample (see Braun et al., 2019). Accuracy in radial strain measurement is here of utmost importance so as to ensure satisfactory zero lateral strain during heating.

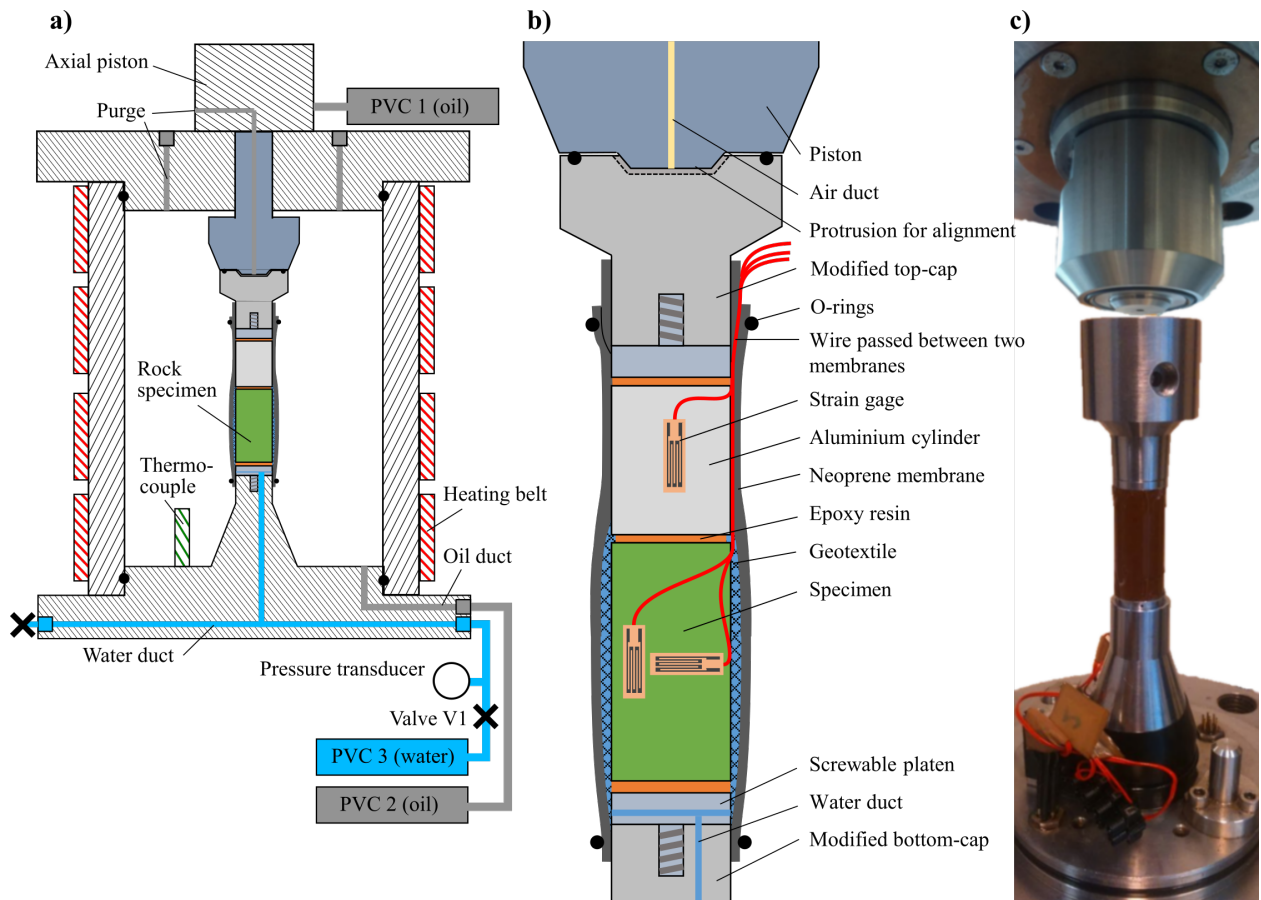


**Fig. 2** a) Schematic view of the triaxial cell. b) Zoom on the specimen assembly with novel extension modifications, permitting to maintain pore pressures larger than the axial total stress through glued connections, while saturation and drainage is achieved through lateral geotextiles. c) Photo showing a dummy specimen mounted with bottom and top caps and the axial piston. The aluminium force transducer is not shown in the photo.

### 2.1 Zero radial strain condition

The zero radial strain condition was achieved through a servo-controlling routine programmed in the LabView software. The routine couples the strain measurements and the cell pressure PVC. Since the cell temperature changes during a test, it is required to correct the measured strains in real-time for thermally induced measurement errors. Following a correction method presented by Braun et al. (2019), a reference gage on a piece of steel 316L was placed in the triaxial cell next to the tested specimen. Doing so, thermal and mechanical strains on a reference material can be recorded. By knowing the thermal expansion coefficient and compressibility of steel 316L, the errors induced by any changes in cell temperature, room temperature, and confining pressure, can be determined as the difference between the measured reference strain and the calculated steel strain. This error was then subtracted from the strain measurements on the specimen. Braun et al. (2019) checked the quality of the thermal strain measurements by testing a specimen of aluminium alloy 2011 under thermal loads. A linear thermal expansion coefficient of the aluminium specimen of  $2.30 \times 10^{-5} \text{ }^\circ\text{C}^{-1}$  was evaluated after correction, which fairly well corresponded with that provided by the manufacturer.

During the laterally constrained heating tests, the corrected lateral strains were monitored, which were maintained at zero value through a partial-integral-derivative (PID) software controller. This servo-control routine calculated the required lateral stress increment, which was then transmitted to the PVC to change the confining stress accordingly. The pressure applied by the axial PVC was simultaneously controlled in order to maintain constant the axial stress. Tuning of the PID controller parameters was carried out before the tests. It was possible to adapt them during the tests, so as to ensure a fast response of the confining PVC and to avoid overshoot and oscillations. The PID routine was executed in intervals of 30 seconds, which proved being sufficiently fast with respect to the adopted heating rate of maximum 10 °C/h. The derivative part of the PID was not necessary to achieve precise control.

## 2.2 Application of tensile axial stress

The main issue met in tension tests in triaxial cells for soils and rocks is the loss of contact between the axial piston and the top cap, once the axial stress becomes smaller than the radial one (i.e. the confining pressure). Donaghe and Chaney (1988) presented a review of the different available systems to avoid this loss of contact in the case of soil testing. They mention screw connections, resin pot systems or a suction cap. The former two methods are difficult to implement when the piston is not easily accessible once the contact with the top cap is made. The suction cap, however, allows closing the cell and moving the piston downwards. Once in contact, a certain surface between the top cap and piston is isolated from the confining stress by means of a rubber membrane. By ensuring a lower pressure than the cell pressure within this surface, and given that the isolated surface is larger than the specimen cross section, the confining pressure keeps the two pieces compressed together. This allows one to transmit tension to the specimen. In the presented system, the connection between the piston and the top cap was based on the principle of a suction cap, by using a flat disc shaped volume isolated by means of an O-ring and connected to atmospheric pressure (Fig. 2b,c). As required, the isolated volume has a base surface larger than the specimen cross section. As seen in Fig. 2b,c, a protrusion in the piston ensures alignment of cap and piston.

Another issue is the loss of contact between top cap and specimen, once the pore pressure becomes equal to the total axial stress. Pore pressures higher than the axial stress cannot be maintained in a device without adequate modifications. A comprehensive overview of different methods to overcome this problem has been given by Perras and Diederichs (2014). They recalled that the two main techniques for direct tensile testing consisted either in attaching the specimen ends to the load frame (by using grips or by gluing, cf. Fairhurst, 1961; Hawkes and Mellor, 1970), or in modifying the sample shape to a so-called dog-bone shape (Hoek, 1964; Brace, 1964). The latter method is not recommended for weak rocks such as claystones, as these materials would not withstand the required shaping process in lathe (Perras and Diederichs, 2014). The former method of gluing or gripping specimen has the advantage that conventional cylindrical specimens can be used. Hawkes and Mellor (1970) have shown that strain inhomogeneities could be reduced, when the specimen was glued only on its end surfaces and not along lateral sections. It was still likely that failure occurred close to the glued end surfaces. In the presented device, the specimen and the caps were therefore glued together by tensile-resistant epoxy resin.

Moreover, an internal axial force transducer was integrated between the specimen and the top cap. Given that no convenient 20 mm diameter force gage was commercially available, a cylindrical aluminium (alloy 2011) piece of 30 mm height and 20 mm diameter was equipped with an axial strain gage (Fig. 2b). This force transducer was previously calibrated, taking into account its thermal dilation.

In the final assembly (Fig. 2b), the aluminium cylinder was glued on top of the specimen. Afterwards, two specially designed screw-able disk-shaped steel platens were glued onto the top of the force transducer and onto the bottom end-surface of the specimen. A two-component epoxy resin (Araldite 2014, Huntsman brand) was used, with a tensile strength of 26 MPa, much larger than the expected strength of the tested specimens. Its glass transition temperature, up to which the resin maintains its original strength, is 80°C. This



temperature that was not exceeded during the tests. Once the resin hardened, the assembly was screwed to the bottom cap, which was fixed to the triaxial cell. The top cap was also screwed onto the assembly, allowing us to maintain tensile stresses. The drainage lines drilled into the bottom platten were connected via the top and bottom cap to a PVC that controls the pore pressure. Since the top and bottom surfaces of the specimen have been made impermeable by impregnating with epoxy resin, drainage had to be ensured by means of a geotextile wrapped around the specimen. The geotextile was connected to the lateral drainage line of the top and bottom platens. Monfared et al. (2011b) have verified that these geotextiles remain permeable even under high confining pressure. A neoprene membrane was then put over the specimen and the geotextile, isolating the confining fluid (silicone oil) from the pore fluid.

The system was developed for specimens with a reduced diameter of 20 mm so as to enable faster drainage and saturation (see Belmokhtar et al., 2018). The drainage length corresponds to the specimen radius of 10 mm and the height of the specimens was close to 35 mm.

### 2.3 Calibration of the drainage system

Ghabezloo and Sulem (2010) summarized the different properties of the drainage system, which are the volume of the drainage system  $V_L$ , its compressibility  $c_L$  due to pressure changes in the drainage system  $p_L$ , the compressibility  $\kappa_L$  due to radial confining pressure changes  $d\sigma_{rad}$ , and the bulk thermal expansion coefficient  $\alpha_L$  under a temperature change  $dT$ . The change in volume of the drainage system can hence be expressed as:

$$\frac{dV_L}{V_L} = c_L dp_L + \alpha_L dT - \kappa_L d\sigma_{rad} \quad (1)$$

with the different parameters defined as:

$$c_L = \frac{1}{V_L} \left( \frac{\partial V_L}{\partial p_L} \right)_{T, \sigma_{rad}} \quad (2)$$

$$\alpha_L = \frac{1}{V_L} \left( \frac{\partial V_L}{\partial T} \right)_{p_L, \sigma_{rad}} \quad (3)$$

$$\kappa_L = -\frac{1}{V_L} \left( \frac{\partial V_L}{\partial \sigma_{rad}} \right)_{T, p_L} \quad (4)$$

Pseudo-undrained conditions are here defined as a constant sum of fluid mass  $dM_f = dM_s + dM_L = 0$  (where  $M_s = m_f V_s$  is the fluid mass in the specimen,  $m_f$  the specimen fluid mass per unit volume,  $V_s$  the specimen total initial volume,  $M_L = V_L \rho_L$  the fluid mass in the drainage system and  $\rho_L$  the density of the fluid in the drainage system). Rewriting the equations of Ghabezloo and Sulem (2010), one obtains:

$$V_L \rho_f [(c_L + c_f) dp_L + (\alpha_L - \alpha_f) dT - \kappa_L d\sigma_{rad}] + V_s dm_f = 0 \quad (5)$$

where  $\rho_f$ ,  $c_f$  and  $\alpha_f$  are the porefluid density, compressibility and bulk thermal expansion coefficient, respectively. In the presented experimental configuration drainage occurs through the lateral specimen surface, therefore the fluid pressure in the drainage system  $p_L$  is equal to the specimen pore pressure on this surface.

Calibration tests were carried out to characterize the properties of the drainage system, assuming that they are constant with stress, pore pressure and temperature. To this end, a steel dummy specimen with zero porosity ( $dM_s = 0$ ) was installed. Saturating the empty drainage system with water provided  $V_L = 3500 \text{ mm}^3$ . Pore pressure changes were applied, while measuring  $dV_L$  with PVC3, which allowed us to calculate  $c_L = 1.33 \text{ GPa}^{-1}$ . Changing the radial stress and measuring the pore pressure change in a closed drainage system resulted in  $\kappa_L = 0.44 \text{ GPa}^{-1}$ . The parameter  $\alpha_L = 0.79 \times 10^{-4} \text{ }^\circ\text{C}^{-1}$  was determined by recording pore pressure changes during temperature cycles.

### 3 Specimen characterization and preparation

The specimens of the COx claystone come from horizontal cores (EST 53650 and EST 57185) extracted at a depth of 490 m in the Bure URL. The clay content of the COx claystone at this level is around 42 %, with an average porosity of 17.5 % and an average water content of 7.9 % (Robinet et al., 2012; Conil et al., 2018). The in situ stress conditions were measured by Wileveau et al. (2007), with a vertical and a minor horizontal total stress of around 12 MPa, a major horizontal stress of around 16 MPa and a hydrostatic pore pressure of about 4.9 MPa.

Avoiding the desaturation and mechanical damage of cores is an important concern, since the claystone mechanical properties should be kept as close as possible to the natural ones. Shales and claystones are known to be particularly sensitive to changes in water content (Chiarelli et al., 2003; Valès et al., 2004; Zhang and Rothfuchs, 2004; Pham et al., 2007; Zhang et al., 2012), that may occur during the successive processes of coring, storage, transportation and trimming of laboratory specimens (Chiu et al., 1983; Monfared et al., 2011a; Ewy, 2015; Wild et al., 2017). Great attention has hence to be paid to preserve the initial water content of the cored specimens. To avoid any contact with water, Andra is used to carry out coring with air-cooling, prior to sealing the extracted cores in so-called T1 cells (Conil et al., 2018). T1 cells accommodate a 320 mm long COx core with 80 mm diameter, previously wrapped in aluminium foil and in a latex membrane to avoid drying. A larger diameter PVC tube is placed around the core and cement is cast in the annulus between the membrane and the tube, creating a rigid mechanical protection. After cement hardening, a metal spring is used to constrain the core along the axial direction.

Once arrived in the laboratory, T1 cells were opened and the cores were immediately covered by a layer of paraffin wax, so as to prevent drying during the trimming process. Cylindrical proofs of 20 mm diameter were drilled perpendicular to the bedding plane by means of a diamond coring bit cooled by compressed air. Note that according to Bažant's theory on the size effect in fracture mechanics, the strength of a rock specimen decreases with its structural size. Moreover, there is the possibility of a statistical size effect, meaning that the probability for encountering heterogeneities of low strength increases with increasing sample size (Bažant, 1984). Such effects couldn't be identified in this study since only 20 mm diameter samples were tested. All samples were oriented with their axis perpendicular to bedding. This facilitates the application of the in situ condition of zero horizontal strain (along the bedding plane) and constant overburden pressure perpendicular to bedding. Such in situ condition favours the tensile failure along the weak bedding plane. This orientation has also the particularities that: a) The tensile fracture direction imposed by the experimental conditions coincides with the bedding plane. b) Radial strains in the direction parallel to bedding are uniform. If the sample is cored along the bedding plane, it would deform non-uniformly in radial directions in triaxial tests, due to thermo-poro-elastic anisotropy. In this case, one would need three orientations of strain gages: axial parallel to the bedding plane, radial parallel to the bedding plane, and radial perpendicular to the bedding plane. Zero radial strain conditions in this configuration would only be possible, if the radial anisotropy of thermal dilation and of mechanical contraction is the same. In the next step, the cylinders were cut at desired length (30 - 40 mm) by using a diamond string saw, to obtain parallel end surfaces. The specimens were afterwards wrapped in an aluminium foil and covered by a mixture of 70 % paraffin and 30 % vaseline oil, and stored until running the tests. Small cuttings of the cores were taken after opening the core, to conduct a petrophysical characterisation (Tab. 2). The volume of the cuttings was measured by hydraulic weighting in petroleum, while the dry density was obtained after oven drying 24 h at 105 °C. A solid density of 2.69 Mg/m<sup>3</sup>, provided by Andra, was adopted to calculate the porosity  $\phi$  and the degree of saturation  $S_r$ . The specimen suction  $s$  was determined by using a chilled mirror tensiometer (WP4C, Decagon brand). As seen in Tab. 2, the high degrees of saturation (92.5 % and 95.3 %) and low corresponding suction values (24.2 and 17.4 MPa) indicate a good conservation of the cores and a satisfactory sample quality.

Once removed from storage and unwrapped from aluminium foil and paraffin, the lateral surfaces of the specimen were protected from drying by wrapping them in an adhesive tape. To ensure correct axial alignment between the specimen and the end platens, the specimen was placed in a V-block with clamp holders (Fig.

**Table 2** Mean and standard deviation (in brackets) of petrophysical measurements done on cuttings of two COx cores.

Core	#	$\rho$ [g/cm <sup>3</sup> ]	$\rho_d$ [g/cm <sup>3</sup> ]	$\phi$ [%]	$w$ [%]	$S_r$ [%]	$s$ [MPa]
EST 53650	1	2.37 (0.00)	2.22 (0.01)	17.9 (0.2)	7.5 (0.1)	92.5 (0.8)	24.2 (2.1)
EST 57185	2	2.38 (0.00)	2.21 (0.00)	18.2 (0.2)	7.9 (0.1)	95.3 (0.7)	17.4 (0.1)

3a) and a layer of epoxy resin was applied to both end surfaces. It was observed that the epoxy resin bonded very well to the claystone, provided that the sample surfaces were previously cleaned from dust by wiping with a paper towel. Bonding the epoxy resin to the surfaces of the metal platens required more caution: the surfaces had to be previously roughened with coarse sand paper and wiped with acetone to remove any dirt or grease. The top and bottom platens were affixed to the specimen with the resin and fastened with clamp holders. To achieve full bonding at room temperature, the epoxy resin had to cure for about 20 h. The assembly was then taken from the V-block, the adhesive tape removed and the two strain gages glued to the specimen at mid-height, along the axial and radial directions (Fig. 2b). A layer of geotextile was wrapped around the specimen, while ensuring contact between the geotextile and the outlets integrated in the bottom platen. Two neoprene membranes were superposed over the geotextile, as indicated in Fig. 3b. The strain gages wires were passed through a section where the membranes overlapped, and sealed with neoprene glue.

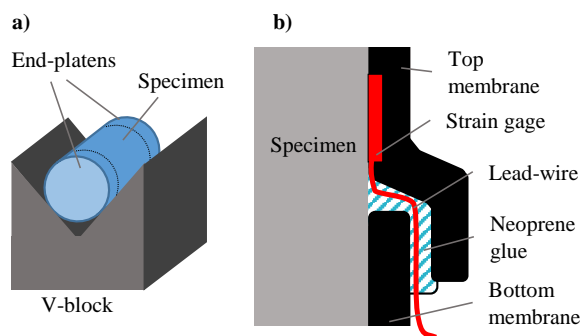


**Fig. 3** a) Attaching the end platens to the specimen using epoxy adhesive, placed in a V-block to ensure axial alignment; b) schematic cut to illustrate the layout of two overlapping membranes to pass-through strain gage wires.

In order to prevent any contact of the sample with water before applying the confining stress, to avoid excessive swelling, the drainage ducts were flushed with air. The specimen was installed in the triaxial cell and connected to the top and bottom caps, by using the screw connections on the two end platens. O-rings were put around the membrane to prevent any leaks on both top and bottom caps. Once the strain gage wires were connected to the data acquisition system, the cell was closed, filled with silicone oil and wrapped by the heating belt to enable temperature control.

#### 4 Experimental results

In the following sections, the notation of Terzaghi effective stress is used to analyse stress states during experiments. The effective stress  $\sigma'_i$  in a direction  $i$  is obtained by  $\sigma'_i = \sigma_i - p_f$ , where  $\sigma_i$  is the total stress

**Table 3** Properties of the specimens measured during the experimental programme, where  $\sigma$  is the isotropic confining stress,  $\varepsilon_{\text{hyd}}$  is the swelling strain during hydration,  $\gamma_t$  the measured fracture angle with respect to the horizontal bedding plane.

Sample	Core	Saturation		Initial state				Failure					
		$\sigma$ [MPa]	$\varepsilon_{\text{hyd}}$ [%]	$T$ [°C]	$\sigma'_z$ [MPa]	$\sigma'_h$ [MPa]	$p_f$ [MPa]	$T$ [°C]	$\sigma'_z$ [MPa]	$\sigma'_h$ [MPa]	$p_f$ [MPa]	$\varepsilon_z$ [%]	$\gamma_t$ [°]
EXT1	2	8	0.2	25.0	7.7	6.9	4.9	61.9	-3.6	5.5	19	-0.36	2
EXT2	2	5	0.21	25.0	2.7	3.5	2.1	53.4	-2.4	4.8	7.9	-0.20	18
EXT3	1	12	0.64	35.0	3.2	8.4	4.0	63.5	-3.0	9.6	7.8	-0.33	7

and  $p_f$  the pore pressure. As seen in Tab. 3, three tests were conducted under different levels of radial effective stress so as to investigate the effect of radial effective stress on the THM stress-strain behaviour and thermal failure of the COx claystone. Specimen EXT1 was tested starting from an isotropic effective stress state close to the in situ one ( $\sigma'_z = 7.7$  MPa,  $\sigma'_h = 6.9$  MPa and pore pressure  $p_f = 4.9$  MPa). EXT2 was started at a lower isotropic effective stress ( $\sigma'_z = 2.7$  MPa,  $\sigma'_h = 3.5$  MPa and  $p_f = 2.1$  MPa), while EXT3 was started at reduced axial effective stress but similar radial effective stress as EXT1 ( $\sigma'_z = 3.2$  MPa,  $\sigma'_h = 8.4$  MPa and  $p_f = 2.1$  MPa).

In tests EXT1 and EXT2, the cell was first brought to a constant initial temperature of 25°C, whereas tests EXT3 was brought at 35°C. The specimens were submitted to the target isotropic confining stress (5, 8 and 12 MPa, respectively, see Tab. 3) at a loading rate of 0.1 MPa/min. The drainage lines were previously dried and put under a vacuum of -80 kPa. Once the target confining pressure reached, the drainage lines were saturated with a synthetic pore water under a pressure of 100 kPa. The composition of this synthetic pore water was similar to that of the natural COx pore water, according to a composition provided by Andra, which consists of 1.95 g NaCl, 0.13 g NaHCO<sub>3</sub>, 0.04 g KCl(2H<sub>2</sub>O), 0.63 g CaSO<sub>4</sub>(7H<sub>2</sub>O), 1.02 g MgSO<sub>4</sub>(2H<sub>2</sub>O), 0.08 g CaCl<sub>2</sub> and 0.7 g Na<sub>2</sub>SO<sub>4</sub> per litre of water. The applied back pressure of 100 kPa was chosen small enough to ensure a negligible decrease in effective stress and to minimize the poroelastic response of the claystone. Swelling strains due to hydration stabilized after about two days, with a maximum value  $\varepsilon_{\text{hyd}} = 0.64\%$  observed for sample EXT3 under 12 MPa (see Tab. 3). This order of magnitude is comparable to that observed by Belmokhtar et al. (2017b); Braun et al. (2021b). After hydration, the piston was brought in contact with the specimen and the desired initial values of the lateral stress ( $\sigma'_h$ ), axial stress ( $\sigma'_z$ ) and pore water pressure ( $p_f$ ) were applied (see Tab. 3). It is assumed that hydraulic equilibrium was achieved when reaching stable deformations.

The thermal extension tests were started by closing the drainage valve V1 (Fig. 2a) and heating the cell with a constant rate of to 10 °C/h for samples EXT1 and EXT3, and 5 °C/h for sample EXT2. Fig. 4 shows the relatively constant rates of temperature elevation, while, due to some technical difficulties in the heating system, heating stopped for a brief time in experiments EXT1 after 4.1 hours and EXT2 after 3.2 hours. In both cases, the desired rate was recovered afterwards. During heating, the servo-control of the confining pressure was switched on to maintain radial strains at zero, while the hydraulic pressure in PVC1 was programmed to keep a constant vertical stress.

Figure 5a presents the data of test EXT1 in terms of applied total stress changes and measured pore pressure changes, with respect to increased temperature. The resulting measured strains in axial and radial direction are plotted in Fig. 5b. The data confirms that the servo-control of zero radial strain could be achieved in the novel device. Note that due to the friction of the sealing gaskets within the axial piston housing, the axial stress on the specimen did not remain constant, even though the pressure applied by PVC1 (Fig. 2a) was stable. Nevertheless, these axial stress changes were recorded by the integrated aluminium force transducer (except in EXT2, where the transducer failed). The direct measurement from the internal force transducer shows some irregularities and step changes between a minimum axial stress of 10.0 MPa and a maximum value of 15.5 MPa from the initial value of 12.6 MPa. This results in an uncertainty of approximately  $\pm 3$  MPa on the axial stress measured by PVC1. These stress variations are most likely due to the changes in radial stress and temperature,

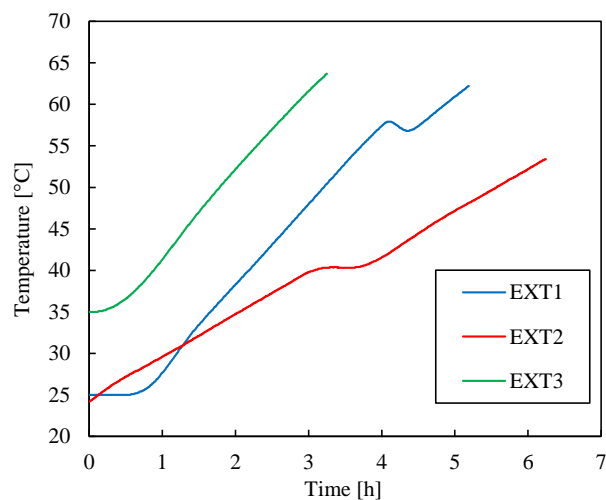


Fig. 4 Imposed temperature changes with respect to time, applied during the heating tests.

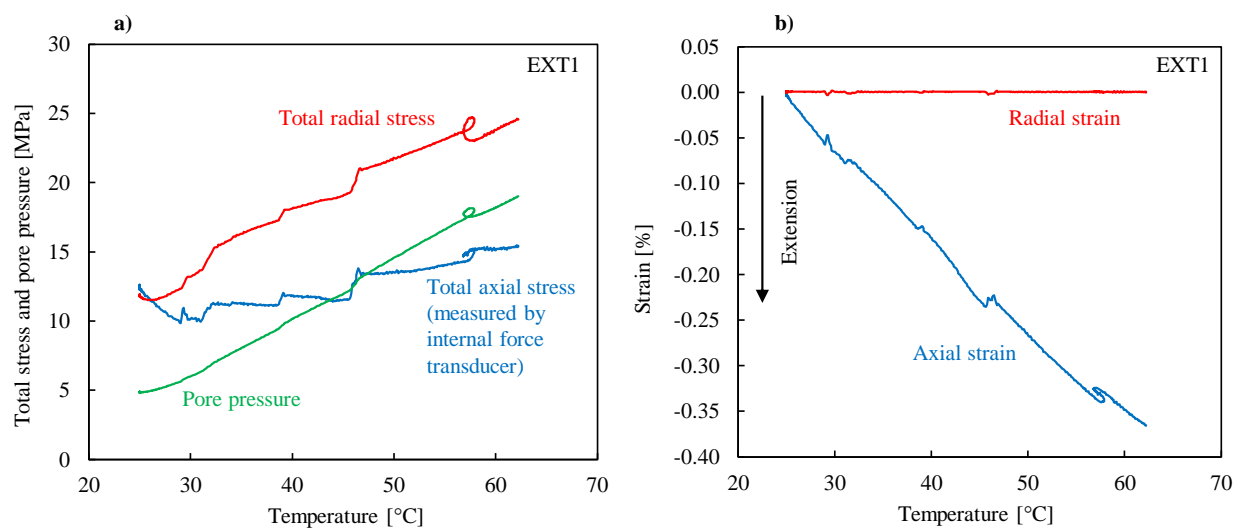
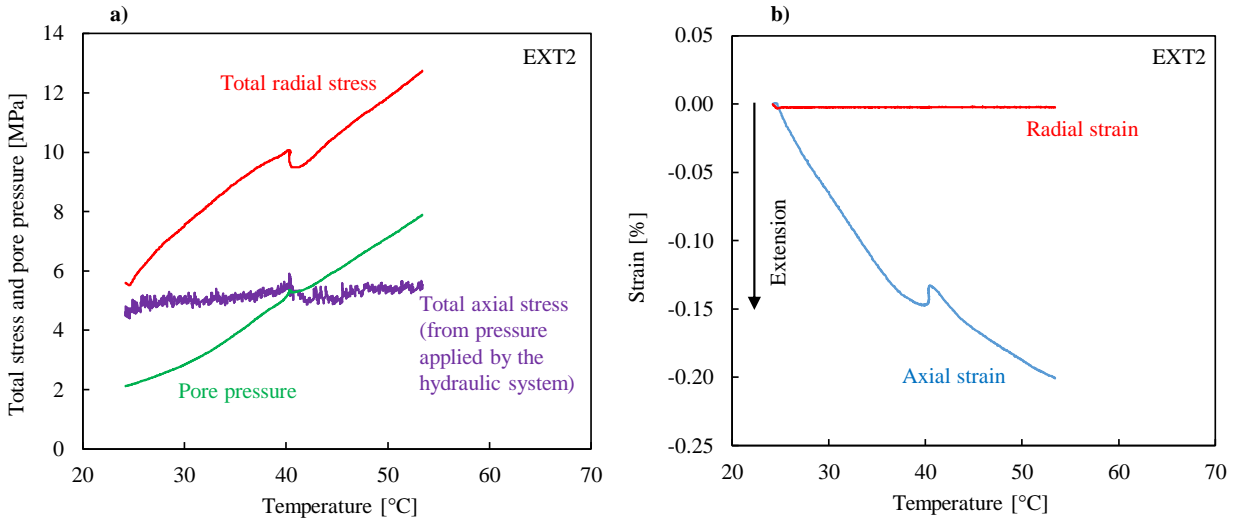


Fig. 5 Test EXT1: a) Total axial stress (measured by force sensor gage and desired to be kept constant by PVC1), total radial stress (servo-controlled by PVC to constrain zero radial strain) and thermally induced pore pressure. b) Radial strains which were maintained null by servo-controlling the confining pressure, and axial strains showing a specimen extension.

which affect the movement or static rest of the axial piston, given by the friction of its sealing components. Unsurprisingly, it is observed that an increase in radial stress is necessary to keep the radial strain to zero during heating. Increasing radial stress compensates the lateral thermal expansion of the saturated specimen. Slight irregularities observed in the axial extension strain (Fig. 5b) are a consequence of those observed in the axial strain control (Fig. 2a). Note that the changes in axial strain are fairly linear until the maximum extension ( $-0.36\%$ ) at the temperature at which thermal failure occurred ( $61.9\text{ }^{\circ}\text{C}$ ). A linear increase in pore pressure from  $4.9\text{ MPa}$  to a maximum of  $19.0\text{ MPa}$  at  $61.9\text{ }^{\circ}\text{C}$  is also observed (Fig. 5a, Tab. 3). Interestingly, all curves show a loop corresponding to the short temperature drop that occurred at  $58\text{ }^{\circ}\text{C}$ .



**Fig. 6** Test EXT2: a) Total axial stress (measured by PVC1 due to failure of the axial force sensor gage), total radial stress (servo-controlled by PVC to constrain zero radial strain) and thermally induced pore pressure. b) Radial strains which were maintained null by servo-controlling the confining pressure, and axial strains showing a specimen extension.

The control of zero radial strains was also ensured in test EXT2 (Fig. 6). In this test, the internal axial force sensor malfunctioned, therefore only the less precise external axial stress measurement obtained by PVC1 are shown. Note that this axial stress includes the significant uncertainty of  $\pm 3$  MPa. The maximum temperature at thermal failure was  $53.4$  °C, with a maximum axial extension at  $\varepsilon_z = -0.20$  %. The pore pressure increased fairly linearly from  $2.1$  MPa to a maximum of  $7.9$  MPa (Fig. 6a, Tab. 3). The plateau observed at  $40.5$  °C in the applied temperature (Fig. 4) caused a perturbation in the otherwise linear behaviour. The nonlinear temperature evolution produced a temporary decrease in total radial stress, axial compaction and pore pressure stabilization, followed by a recovery of the rates observed before the perturbation.

In experiment EXT3 (Fig. 7), one can observe a decrease in total axial stress from the initial value of  $7.2$  MPa down to  $4.6$  MPa at  $53$  °C, followed by a stabilization with a slight increase above  $53$  °C, up to  $63.5$  °C, at which thermal pressurization failure occurred (Tab. 3). The axial stress variation lies within the uncertainty of the external control system due to piston friction ( $\pm 3$  MPa). A clear coupling between the axial and the radial stress is again observed. The increase in pore pressure is almost linear, like in test EXT1. A plateau in pore pressure changes is observed between  $47$  and  $51$  °C, which is supposed to be due to non-linear material behaviour. Zero radial strain was again achieved, while the axial strains decreased down to  $\varepsilon_z = -0.34$  %.

Figure 8 presents the changes in Terzaghi effective stress with increased temperature. The linear decrease of the effective axial stress is related to the linear increase in pore pressure observed in Figs. 5 to 7. The temperatures at which axial effective tensile stress (negative effective stress) starts to be applied are quite comparable in all three cases, at  $43.5$  °C for EXT1 and EXT3 and  $40.5$  °C for EXT2. Finally, as shown in Tab. 3, thermal tensile failure is observed at  $-3.6$  MPa and  $61.9$  °C (with a radial effective stress of  $5.5$  MPa) for EXT1, at  $-2.4$  MPa and  $53.4$  °C (with a radial effective stress of  $4.8$  MPa) for EXT2 and  $-3.0$  MPa at  $63.5$  °C (with a radial effective stress of  $9.6$  MPa) for EXT3. Interestingly, the changes in effective radial stress are rather small and limited between the boundary values ( $5.5$  and  $8.3$  MPa for EXT1,  $3.5$  and  $5.1$  MPa for EXT2 and  $8.5$  and  $10.2$  MPa for EXT3).

The thermo-hydro-mechanical stress paths of the three tests are represented in Fig. 9 in terms of radial ( $y$ -axis) and axial ( $x$ -axis) principal effective stress. The curves indicate that there is no clear dependency of the thermal tensile failure stress with respect to the applied effective radial stress.

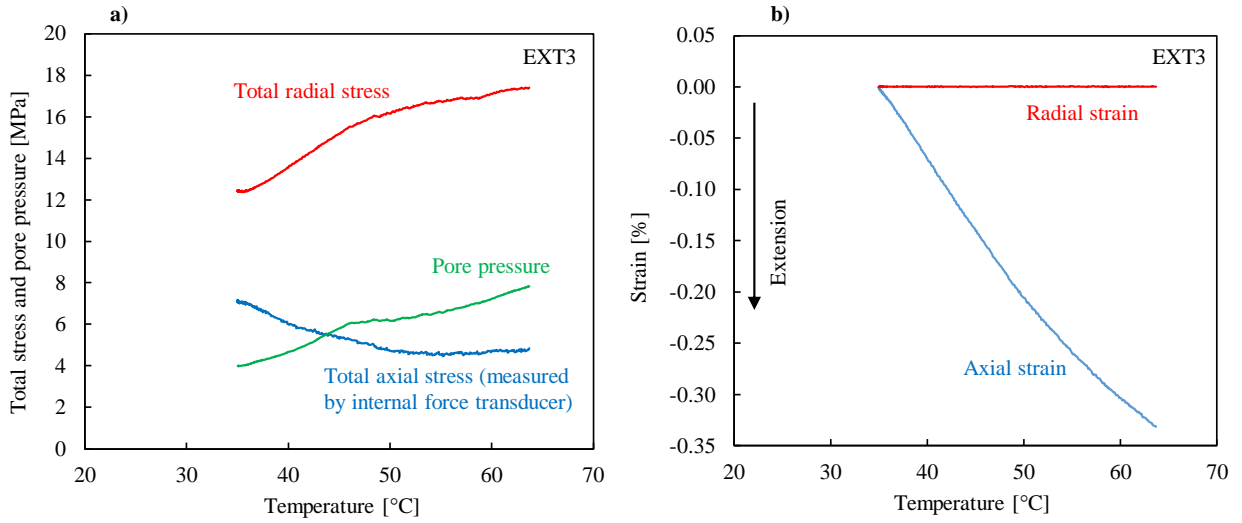


**Fig. 7** Test EXT3: a) Total axial stress (measured by force sensor gage and desired to be kept constant by PVC1), total radial stress (servo-controlled by PVC to constrain zero radial strain) and thermally induced pore pressure. b) Radial strains which were maintained null by servo-controlling the confining pressure, and axial strains showing a specimen extension.

Note that the aim of this study is to reproduce stress paths similar to the ones in situ, in order to obtain a failure criterion close to the in situ conditions. Since laboratory and in situ conditions are hardly identical, undrained conditions are assumed in this study. These are neither exactly met in situ due to the complex 3D drainage conditions, nor in the laboratory due to the dead volume of the drainage system. In consequence, the failure criterion measured in this study has to be compared to the results of numerical simulations, which take into account complex 3D conditions of temperature, stress and drainage.

## 5 Thermo-poroelastic analysis

Due to the complex nature of the transversely isotropic coupled THM behaviour, it is difficult to directly evaluate material parameters from the test data. In the presented complex loading paths, a variety of constitutive behaviours (elasticity, plasticity, viscosity, etc.) could be involved. For the following calculations, elastic behaviour is assumed. This simple analysis shall provide a basis for future in-depth modelling. In the following, a transversely isotropic THM model is used to simulate the conducted experiments. Material parameters are taken from different previous studies. The analysis is presented in two steps: First, an element test is simulated in drained conditions, where the experimentally measured pore pressure is imposed. Only a single material point is simulated, therefore the system can be solved in an analytical way or using finite differences, if nonlinear parameters are considered. The simulated stress-strain response is compared with the experimental results, to calibrate thermo-poroelastic material properties. If one wants to model the material behaviour in undrained conditions in a second step, the presence of the dead volume of the drainage system has to be taken into account. This dead volume induced pseudo-undrained conditions, which can be simulated based on previous calibration tests (Sec. 2.3).

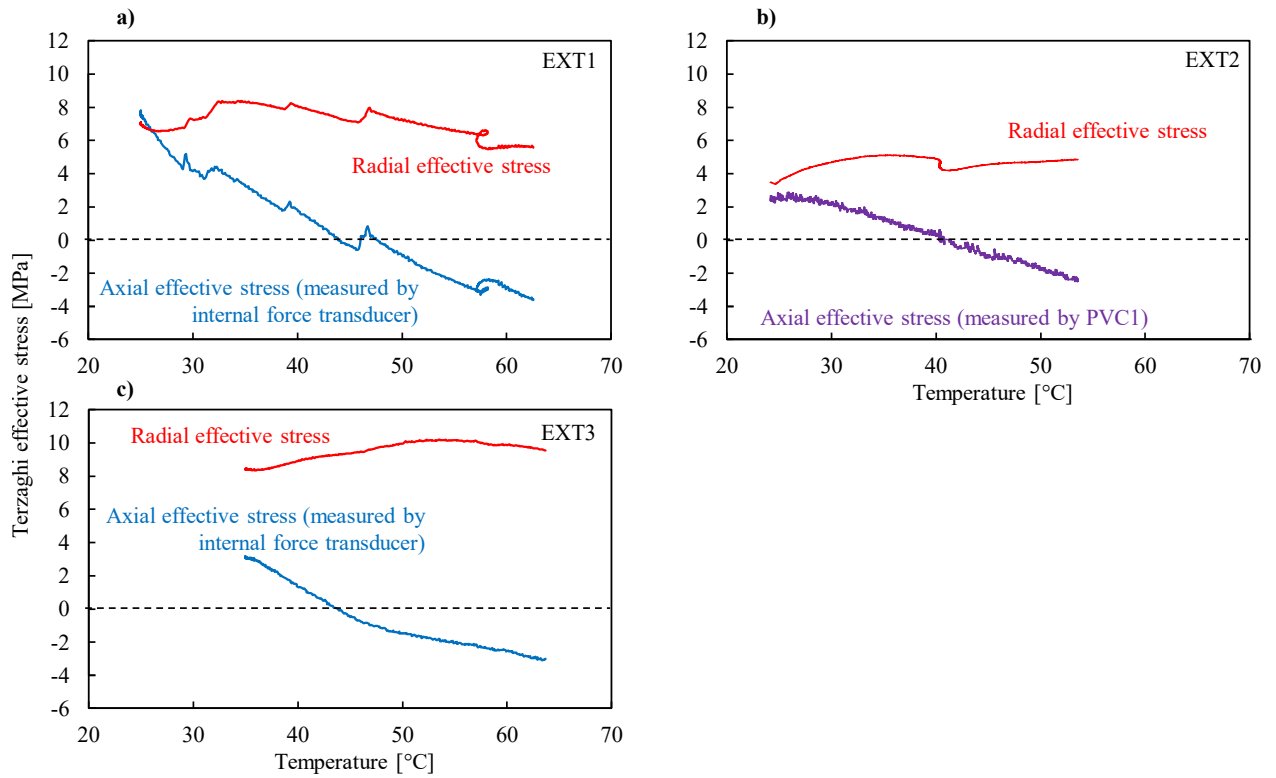


**Fig. 8** Changes in Terzaghi effective stresses with temperature during the three heating tests, where negative stresses represent effective tension. In test EXT2 the internal force sensor malfunctioned and stresses measured by the external transducer are shown instead.

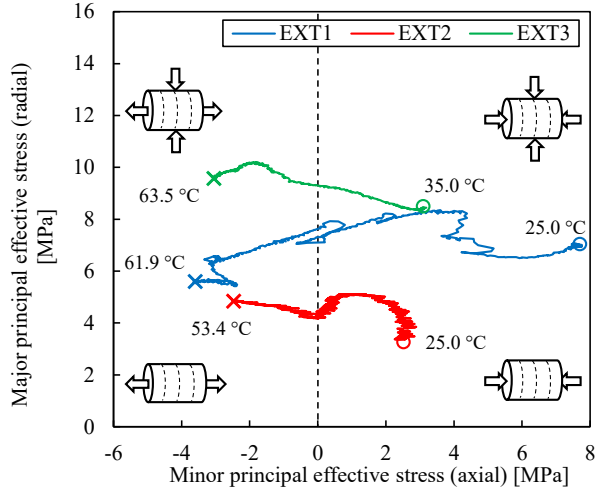


**Fig. 9** Principal (Terzaghi) effective stress paths for all three specimens tested. Circles indicate the initial stress state and temperature, while crosses mark the specimen failure with their respective temperature.



### 5.1 Transversely isotropic thermo-poroelastic framework

The thermal properties and THM couplings are analysed within the thermo-poroelastic constitutive equations, presented among others in the works of Biot and Willis (1957), Palciauskas and Domenico (1982) and Coussy (2004). The thermo-poromechanical formulations are written for a Representative Elementary Volume (REV) of the porous material. A relationship between strain  $\varepsilon_i$ , total stress  $\sigma_i$ , pore pressure  $p_f$  and temperature  $T$  is expressed within this framework, as:

$$d\varepsilon_i = C_{ij} (d\sigma_j - b_j dp_f) - \alpha_{d,i} dT \quad (6)$$

where  $\sigma_j$  is composed of the normal stresses and shear stresses in different directions:

$$\sigma_i = [\sigma_x, \sigma_y, \sigma_z, \sigma_{xy}, \sigma_{yz}, \sigma_{zx}]^\top \quad (7)$$

The strains in different direction are contained within the strain vector  $\varepsilon_i$ :

$$\varepsilon_i = [\varepsilon_x, \varepsilon_y, \varepsilon_z, \varepsilon_{xy}, \varepsilon_{yz}, \varepsilon_{zx}]^\top \quad (8)$$

In terms of material properties, one has to define the Biot effective stress coefficients  $b_i$ , the compliance matrix  $C_{ij}$  and the thermal expansion coefficients  $\alpha_{d,i}$ .

It has been shown that the COx claystone is transversely isotropic (Plúa et al., 2021b), therefore a simplified set of coefficients is presented (the properties along the directions  $x$  and  $y$  are identical, denoted in the following with a subscript  $h$ ). Like in most claystones, this plane of isotropy corresponds to the bedding plane. According to Cheng (1997), the coefficients of transverse isotropy are recalled here.

The vector  $b_i$  represents the Biot effective stress coefficients in both directions of anisotropy:

$$b_i = [b_h, b_h, b_z, 0, 0, 0]^\top \quad (9)$$

One can also write down the entries of the compliance matrix  $C_{ij}$  as follows:

$$C_{ij} = \begin{pmatrix} C_{11} & C_{12} & C_{13} & 0 & 0 & 0 \\ C_{12} & C_{11} & C_{13} & 0 & 0 & 0 \\ C_{13} & C_{13} & C_{33} & 0 & 0 & 0 \\ 0 & 0 & 0 & 1/2G' & 0 & 0 \\ 0 & 0 & 0 & 0 & 1/2G & 0 \\ 0 & 0 & 0 & 0 & 0 & 1/2G \end{pmatrix} \quad (10)$$

with

$$\begin{aligned} C_{11} &= 1/E_h \\ C_{12} &= -\nu_{hh}/E_h \\ C_{13} &= -\nu_{zh}/E_z \\ C_{33} &= 1/E_z \\ G' &= E_h/(1 + \nu_{hh}) \end{aligned} \quad (11)$$

where  $E_z$  and  $\nu_{zh}$  are the Young modulus and the Poisson ratio perpendicular to the bedding plane, and  $E_h$  and  $\nu_{hh}$  parallel to the bedding plane, respectively.  $G$  describes the independent shear modulus perpendicular to the isotropic plane.

The thermal behaviour is represented by  $\alpha_{d,i}$ , which consists of the two linear drained thermal expansion coefficients perpendicular ( $\alpha_{d,z}$ ) and parallel ( $\alpha_{d,h}$ ) to the bedding orientation:

$$\alpha_{d,i} = [\alpha_{d,h}, \alpha_{d,h}, \alpha_{d,z}, 0, 0, 0]^\top \quad (12)$$

The change of fluid content  $m_f$  is described by Coussy (2004):

$$\frac{dm_f}{\rho_f} = -b_i d\varepsilon_i + \frac{1}{M} dp_f - (b_i \alpha_{d,i} - \phi \alpha_\phi + \phi \alpha_f) dT \quad (13)$$

Here,  $\alpha_\phi$  denotes the bulk thermal expansion coefficient of the pore volume and  $\alpha_f$  the bulk thermal expansion coefficient of the pore fluid. The parameter  $M$  is the Biot modulus, which, according to Aichi and Tokunaga (2012), can be calculated for a saturated transversely isotropic material:

$$\frac{1}{M} = 2(1 - b_h) \left[ \frac{(1 - \nu_{hh}) b_h}{E_h} - \frac{\nu_{zh} b_z}{E_z} \right] + \frac{(1 - b_z)}{E_z} (b_z - 2\nu_{zh} b_h) + \phi \left( \frac{1}{K_f} - \frac{1}{K_\phi} \right) \quad (14)$$

where  $K_f$  the bulk modulus of the pore fluid and  $K_\phi$  the bulk modulus of the pore volume.

## 5.2 Simulation of a heating test with imposed pore pressure

First, the observed claystone behaviour is simulated during extension using the thermo-poroelastic framework discussed in Sec. 5.1. Element tests are modelled with homogeneous pore pressure, temperature, stress and strain distributions. Linear thermo-poroelasticity is considered, therefore the experiments can be reproduced through analytical calculations. Zero lateral deformation, the measured axial stress, the recorded pore pressure changes and the applied temperature are imposed. Constitutive parameters were taken from the literature, summarized in the following: Escoffier (2002) and Belmokhtar et al. (2017b) provided measurements for  $b$  close to 0.9 at effective stresses close to the in situ one (around 9 MPa). Recently, Braun et al. (2021b) estimated the Biot coefficient also for lower effective stress levels, showing that  $b_z$  approaches 1.0 at effective stresses tending to zero. For the following calculations, representing the in situ condition where the mean effective stress decreases, starting from around 8 MPa,  $b_z = b_h = 0.9$  was chosen. The Young modulus  $E_z$  at 8 MPa mean effective stress was determined by Menaceur et al. (2015) and Belmokhtar et al. (2018), with values around 3 GPa, and at lower mean effective stress by Menaceur et al. (2015) and Zhang et al. (2012), with values around 1.0 and 1.5 GPa. For 8 MPa effective mean stress, Braun et al. (2021b) found through a multivariate regression a best-fit value of  $E_z$  close to 2.6 GPa, which was adopted in this calculation. Less data is available for  $E_h$  and the Poisson ratios.  $E_h = 5.7$  GPa and  $\nu_{zh} = 0.11$ , which was measured by Braun et al. (2021b) under 8 MPa effective stress is utilized.  $\nu_{hh} = 0.29$  was given by the Andra database (Guayacán-Carrillo et al., 2017) and confirmed by Braun et al. (2021b). The anisotropic drained thermal expansion coefficients  $\alpha_{d,z} = 0.21 \times 10^{-5} \text{ } ^\circ\text{C}^{-1}$  and  $\alpha_{d,h} = 0.51 \times 10^{-5} \text{ } ^\circ\text{C}^{-1}$  are taken from the experimental results of Braun et al. (2021a) on COx claystone. Moreover, a porosity of 0.18, measured in the present study, is used. It is assumed that all parameters are stress and temperature independent.

Using Eq. (6), one is able to calculate the changes in radial stress and axial strains, based on the applied axial stress, the measured pore pressure and the applied temperature (Fig. 10a-f). The radial strains were kept equal to zero. The strain calculations show a good match with the experimental data, without any parameter fitting necessary. Only the axial strains in EXT3 become significantly nonlinear at around 50 °C, which is not represented by the simulation. This difference could be due to natural variability of the specimens, the occurrence of strain localisation, not detected local strain gages, or induced damage or plastic deformations, which cannot be captured with the linear thermo-poroelastic model. Calculated radial stresses show a general slight underestimation. To get a first estimation of the parameter sensitivity, a preliminary parametric analysis was carried out within the following section.

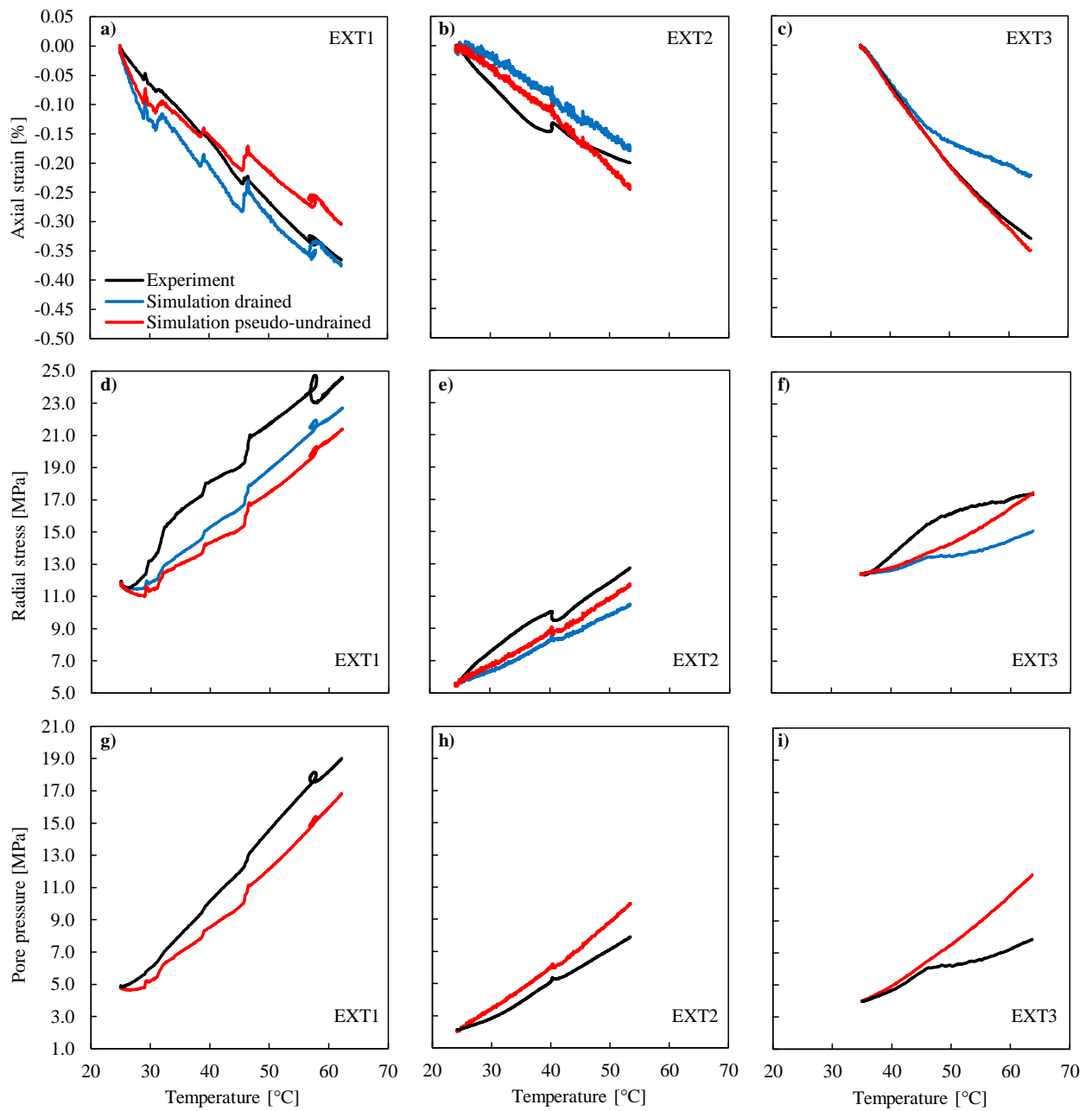


**Fig. 10** Experimental results and calculated behaviour using a thermo-poroelastic model on three extension tests EXT1-3. a) - c) Temperature - axial strain evolution, d) - f) radial stress evolution with temperature and g) - i) thermally induced pore pressure increase. Note that for the simulation in drained conditions, the pore pressure increase from experimental data was imposed.

### 5.3 Simulation of thermal pressurization in pseudo-undrained conditions

To simulate the experiment in pseudo-undrained conditions, the dead volume of the drainage system can be modelled through Eq. (5), using the drainage system properties evaluated in Sec. 2.3. The change of the specimen fluid mass per unit volume is calculated through Eq. (13). A single element test with uniform pore pressure and fluid density within the specimen and the drainage system ( $p_f = p_L$ ,  $\rho_f = \rho_L$ ) is simulated. Next to the properties used in Sec. 5.2, additional parameters concerning the deformations of the pore space and the pore fluid are required in Eq. (13). The Biot modulus is computed through Eq. (14). Moreover, as a first hypothesis, it is assumed that  $K_\phi$  is equal to theunjacketed bulk modulus of 19.7 GPa (Braun et al., 2021b) and  $\alpha_\phi$  is equal to  $2\alpha_h + \alpha_z$ . For the water properties  $\alpha_f$  and  $K_f$ , a dependency on the fluid pressure and temperature is considered, according to IAPWS-IF97 (2008). In consequence, the material response becomes nonlinear, which was simulated using the explicit finite difference method with sufficiently small increments  $dT \leq 0.1$  °C,  $dp_f \leq 0.2$  MPa.

One observes a good simulation of the axial extension strains in Fig. 10a-c, the radial stress change in Fig. 10d-f and the thermally induced pore pressures in Fig. 10g-i. Axial strain changes are well reproduced by the simulation, while radial stresses of EXT1 and EXT2 are slightly underestimated. Calculated pore pressures follow the experimental trend, while they slightly overestimate the result of test EXT1 and underestimate EXT2. The pore pressure increase of EXT3 is significantly overestimated.

Due to the parallel over- and underestimation of experimental pore pressures, an adjustment of the additional parameters  $K_\phi$ ,  $\alpha_\phi$ ,  $\alpha_f$  and  $K_f$  does not improve the fitting. A preliminary parametric analysis was carried out by varying separately each model parameter by 10 % and observing the variation of the final pore pressure in test EXT1. The highest parameter sensitivity was detected for  $b_z$ , which caused a variation of the resulting pore pressure of 7 %. The parameters  $\alpha_f$  and  $\phi$  caused a variation of 4 % and  $E_z$  a variation of 3 %. The variation of other parameters induced a change of  $\leq 1\%$  on the pore pressure result. Also a better fitting of the horizontal elastic properties  $E_h$  and  $\nu_{zh}$ , on which literature data is scarce, could provide better results. For further information on the in situ variability of parameters, the reader is referred to Plúa et al. (2021b).

The set of linear thermo-poroelastic claystone properties used here appears to be sufficient to simulate closely the measure laboratory thermal extension. It has to be noted that non-linear water properties are essential to model thermal pressurization.

## 6 Failure criterion

Based on the stress state measured at tensile failure (Fig. 9), the existing shear failure criterion of the COx claystone is extended. A Mohr-Coulomb (MC) type failure criterion, based on uniaxial and triaxial compression tests on the COx claystone, is given in the Andra database (applied also by Guayacán-Carrillo et al., 2017). The criterion can be transformed to the principal effective stress domain, written as:

$$\sigma'_1 = \frac{1 + \sin \varphi}{1 - \sin \varphi} \sigma'_3 + \frac{2c \cos \varphi}{1 - \sin \varphi} \quad (15)$$

where  $\sigma'_1$  and  $\sigma'_3$  are the major and minor principal effective stresses, respectively. Values for the cohesion  $c = 5.9$  MPa and the friction angle  $\varphi = 23^\circ$  are taken from the Andra database, when the minor effective stress is perpendicular to the bedding plane. This shear failure criterion, displayed in Fig. 11, provides us an unconfined compressive strength  $\sigma_c = \sigma'_1(\sigma'_3 = 0) = 17.8$  MPa. One notes, that the Mohr-Coulomb criterion overestimates the measured strength in tension, and is therefore not applicable in this region.

Hoek and Brown (1980) and Hoek (1983) described the Hoek-Brown (HB) failure criterion, proposed as an empirical relationship for observed shear failure of rock under triaxial compressive stress:

$$\sigma'_1 = \sigma'_3 + \sigma_c \left( m_i \frac{\sigma'_3}{\sigma_c} + 1 \right)^{0.5} \quad (16)$$

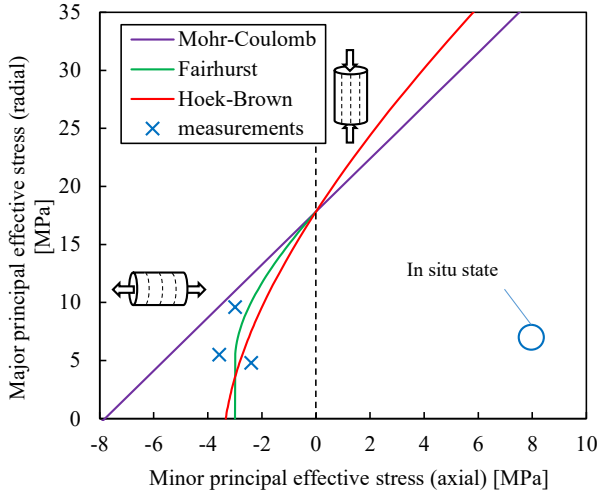


**Fig. 11** Hoek-Brown and Fairhurst's generalized Griffith criterion, adopted for measured tension failure with tension perpendicular to the bedding. The Mohr-Coulomb criterion is obtained from the Andra database, based on shear failure with a major principal stress parallel to bedding

This criterion was fitted for the measured strength in tension. The shear failure region was not investigated here, however  $\sigma_c = 17.8$  MPa from the Andra database can be adopted. A single parameter  $m_i$  had to be fitted, carried out by minimising the sum of squared errors in terms of  $\sigma'_3$ . The best-fit, obtained with  $m_i = 5.15$ , is presented in Fig. 11. Note that the HB criterion was conceived for intact isotropic rock, while the COx claystone is anisotropic (Eberhardt, 2012). For a more versatile form of the HB criterion, the reader is referred to the "generalised" HB criterion (Hoek et al., 1995).

As quoted by Hoek and Martin (2014), the HB criterion can over-estimate the tensile strength of rocks with a low  $m_i$  value. Hoek and Martin (2014) suggest to utilize the Fairhurst generalized Griffith (FG) failure criterion (Fairhurst, 1964) to predict tensile failure. This criterion can be applied in the form of a so-called "tension cutoff" under tensile stresses, combined with a Mohr-Coulomb or Hoek-Brown criterion for shear stresses.

Fairhurst (1964) presented the FG criterion (Griffith, 1924), which is here recalled according to Hoek and Martin (2014):

If  $w(w - 2)\sigma'_3 + \sigma'_1 \leq 0$ , failure occurs when:

$$\sigma'_3 = \sigma_t \quad (17)$$

or when:

$$\sigma'_1 = \frac{(2\sigma'_3 - A\sigma_t)}{2} + \frac{\sqrt{(A\sigma_t - 2\sigma'_3)^2 - 4(\sigma_3'^2 + A\sigma_t\sigma'_3 + 2AB\sigma_t^2)}}{2} \quad (18)$$

where

$$\left. \begin{aligned} A &= 2(w - 1)^2 \\ B &= [(w - 1)/2]^2 - 1 \\ w &= \sqrt{\sigma_c/|\sigma_t| + 1} \end{aligned} \right\} \quad (19)$$

Combined with the Mohr-Coulomb criterion described before, the major principal stress where both criteria coincide at  $\sigma'_3 = 0$ , is the unconfined compressive strength  $\sigma_c = 17.8$  MPa. The remaining coefficient to

be determined for the FG criterion is the tensile strength  $\sigma_t$ , that can be evaluated from the laboratory measurements. A regression by minimizing the orthogonal least square error was used, which provided the best-fit value of  $\sigma_t = 3.0$  MPa (Fig. 11).

Both HB and FG criteria are able to satisfactorily characterize the tensile failure of the COx specimens. Both criteria can be adopted in combination with other criteria for shear failure, such as the MC criterion presented before. The HB criterion fitted for tensile failure was observed to overestimate the shear failure characterized by a MC criterion from the Andra database.

Note that this data was fitted for failure under tension perpendicular to the bedding layer. Both HB and FG criteria account only for isotropic resistance. To consider anisotropic resistance, one would have to modify the criterion by adjusting  $m_i$ ,  $\sigma_t$  or  $\sigma_c$  with respect to the principal loading direction (see also Pardoen et al., 2015; Mánica et al., 2021).

The characteristics evaluated in the thermal extension tests of this study are compared with literature data on other shales and claystones in Tab. 1. One observes that the parameter  $m_i$  ( $\sigma_t = \sigma_c/m_i$ ) for the COx claystone is found within the range of  $m_i \approx 4.0$  (Hoek, 2007) and within the estimated values for other shales and claystones. One notes that the estimated values of  $m_i$  are all somewhat higher than 4.0. The measured tensile resistance of the COx claystone is comparable to that of other shales and claystones, in the range of a few MPa.

The values obtained here by direct tension tests are somewhat higher than those measured by Auvray et al. (2015) indirectly through Brazilian tests. This could be due to difference in testing methods. The samples of Auvray et al. (2015) were saturated under stress, but had to be de-confined for testing, which could result in some damage. Note also, that probably due to their small size, the specimens tested in the present study were prone to breakage during sample preparation. This could have possibly resulted an involuntarily rejection of less resistant or pre-fractured specimens, so that predominantly resistant samples were finally tested.

Auvray et al. (2015) did not note any significant change of tensile resistance on specimens tested at 90 °C, neither could a temperature dependency be observed in this study, due to the scarcity of results.

## 7 Conclusions

A novel triaxial apparatus for investigating the thermal pressurization failure of soft rocks was developed and used on samples of the COx claystone. The challenging conditions, which might occur at mid-distance between two horizontal and parallel micro-tunnels containing high activity exothermic radioactive wastes, are mimicked by the designed device. At this location lateral strains are constrained by symmetry, the overburden stress is constant and undrained heating by the two adjacent micro-tunnels increases the temperature. These loadings submit the claystone to an extension, which could eventually lead to tensile failure.

A triaxial device with simultaneous control of temperature, axial and radial stresses and pore pressure was designed and employed. The lateral strain was kept to zero by servo-controlling the confining stress, while maintaining the axial stress constant through the piston. Axial effective tensile stresses require gluing the top and bottom caps through epoxy resin with a higher tensile strength than the tested specimen. Special bases with screw connections were designed for that purpose. For specimen saturation, it was necessary to implement special drainage ducts and a lateral geotextile. Axial stress was measured internally by a calibrated aluminium force transducer. To achieve precise real-time lateral strain control, measured strains had to be corrected for temperature effects through a dummy strain gage. Attention had to be paid to tuning the proportional parameter of the PID controller, which determines the confining stress response upon radial strain changes. The derivative parameter was not necessary for fast control.

The investigated cylindrical COx specimens of 20 mm diameter and 30 – 40 mm height, cored perpendicular to the bedding plane, were handled with care to avoid drying or swelling. All specimens were saturated under close to in situ effective stress. A series of undrained heating tests with zero radial strain and constant axial stress was carried out on these samples. As expected, an increase in pore pressure due to thermal pressurization

was observed. Constraining the radial strain to zero required a significant increase in radial total stress. Pore pressure and radial stress increased for nearly the same amount, leading to a fairly constant radial effective stress. Axial effective stress decreased continuously until reaching negative values. The recorded axial strains showed a fairly linear extension behaviour. Temperature induced pressurization led to failure, once the limit effective tensile strength of the claystone was reached at values around 3 MPa and temperatures between 53 and 64°C.

The observed strength of COx claystone under tension perpendicular to the bedding plane is overestimated by criteria calibrated on triaxial compression tests. A Hoek-Brown and a Fairhurst generalized Griffith criterion, calibrated on the rock's measured tensile strength, are proposed for a better representation of the failure in the low effective stress regime. The tensile strength parallel to the bedding plane was not measured in this study and might be different to the perpendicular one. Anisotropic resistance could be taken into account by failure criterion parameters which depend on the stress orientation. The size effect on the tensile resistance was not investigated in this study. According to Bažant's theory (Bažant, 1984), the tensile resistance of larger samples might be smaller than the one measured in this study. Also there might be a higher probability for the existence of heterogeneities in larger samples. Future experiments on samples with larger diameter could provide important insight in this regard.

Satisfactory modelling of the experimental response was achieved within a thermo-poroelastic framework, based on thermo-hydro-mechanical parameters of the COx claystone that were previously determined by Braun et al. (2021a,b). Axial strains were well reproduced by the thermo-poroelastic simulation. Only some non-linear behaviour of experiment EXT3 could not be simulated. One could observe that calculated radial stresses of two tests show a slight underestimation of measured behaviour. The simulated pore pressure changes follow in general the experimental trend with no clear over- or underestimation. The pore pressure evolution was found to be most sensitive to the Biot coefficient  $b_z$ , followed by  $\alpha_f$ ,  $\phi$  and  $E_z$ . Note that the adoption of non-linear water properties is essential to model thermal pressurization.

## Conflict of interest

The authors declare that there are no known conflicts of interest associated with this publication.

## References

- Abuel-Naga HM, Bergado DT, Bouazza A (2007) Thermally induced volume change and excess pore water pressure of soft bangkok clay. *Engineering Geology* 89(1-2):144–154
- Aichi M, Tokunaga T (2012) Material coefficients of multiphase thermoporoelasticity for anisotropic micro-heterogeneous porous media. *International Journal of Solids and Structures* 49(23-24):3388–3396
- Akazawa T (1943) New test method for evaluating internal stress due to compression of concrete (the splitting tension test)(part 1). *Journal of Japanese Civil Engineering Institute* 29:777–787
- Andra (2005) Dossier 2005 Argile: Evaluation of the feasibility of a geological repository in an argillaceous formation. URL <http://www.andra.fr/international/download/andra-international-en/document/editions/266va.pdf>
- Armand G, Dewonck S, Bosgiraud JM, Richard-Panot L (2015) Development and New Research Program in the Meuse Haute-Marne Underground Research Laboratory (France). In: *Proceedings of the 13th ISRM International Congress of Rock Mechanics, Montreal, Canada*
- Armand G, Bumbieler F, Conil N, de la Vaissière R, Bosgiraud JM, Vu MN (2017) Main outcomes from in situ thermo-hydro-mechanical experiments programme to demonstrate feasibility of radioactive high-level waste disposal in the Callovo-Oxfordian claystone. *Journal of Rock Mechanics and Geotechnical Engineering* 9(3):415–427, DOI 10.1016/j.jrmge.2017.03.004

- Auvray C, Giot R, Giraud A (2015) Caractérisation géomécanique sur échantillons - Essais de traction indirecte, Andra report. Tech. rep.
- Baldi G, Hueckel T, Pellegrini R (1988) Thermal volume changes of the mineral–water system in low-porosity clay soils. *Canadian Geotechnical Journal* 25(4):807–825
- Bazant ZP (1984) Size Effect in Blunt Fracture: Concrete, Rock, Metal. *Journal of Engineering Mechanics* 110(4):518–535, DOI 10.1061/(asce)0733-9399(1984)110:4(518)
- Belmokhtar M, Delage P, Ghabezloo S, Conil N (2017a) Thermal Volume Changes and Creep in the Callovo-Oxfordian Claystone. *Rock Mechanics and Rock Engineering* 50(9):2297–2309
- Belmokhtar M, Delage P, Ghabezloo S, Tang AM, Menaceur H, Conil N (2017b) Poroelasticity of the Callovo-Oxfordian Claystone. *Rock Mechanics and Rock Engineering* 50(4):871–889
- Belmokhtar M, Delage P, Ghabezloo S, Conil N (2018) Drained Triaxial Tests in Low-Permeability Shales: Application to the Callovo-Oxfordian Claystone. *Rock Mechanics and Rock Engineering* 51(7):1979–1993
- Biot MA, Willis DG (1957) The Elastic Coefficients of the Theory of Consolidation. *Journal of Applied Mechanics* 24:594–601
- Bossart P (2011) Characteristics of the Opalinus Clay at Mont Terri. Mont Terri Project, Wabern Switzerland (3):26
- Brace WF (1964) Brittle fracture of rocks. State of stress in the Earths Crust pp 111–174
- Braun P, Ghabezloo S, Delage P, Sulem J, Conil N (2019) Determination of multiple thermo-hydro-mechanical rock properties in a single transient experiment: Application to shales. *Rock Mechanics and Rock Engineering* 52:2023–2038
- Braun P, Delage P, Ghabezloo S, Sulem J, Conil N (2020) Effect of anisotropy on the thermal volume changes of the Callovo–Oxfordian claystone. *Géotechnique Letters* 10(1):63–66, DOI 10.1680/jgele.19.00045
- Braun P, Ghabezloo S, Delage P, Sulem J, Conil N (2021a) Thermo-Poro-Elastic Behaviour of a Transversely Isotropic Shale: Thermal Expansion and Pressurization. *Rock Mechanics and Rock Engineering* 54(1):359–375, DOI 10.1007/s00603-020-02269-y
- Braun P, Ghabezloo S, Delage P, Sulem J, Conil N (2021b) Transversely Isotropic Poroelastic Behaviour of the Callovo-Oxfordian Claystone: A Set of Stress-Dependent Parameters. *Rock Mechanics and Rock Engineering* 54(1):377–396, DOI 10.1007/s00603-020-02268-z
- Bumbieler F, Plúa C, Tourchi S, Vu MN, Vaunat J, Gens A, Armand G (2021) Feasibility of constructing a full-scale radioactive high-level waste disposal cell and characterization of its thermo-hydro-mechanical behavior. *International Journal of Rock Mechanics and Mining Sciences* 137(November 2020), DOI 10.1016/j.ijrmms.2020.104555
- Carneiro F (1943) A new method to determine the tensile strength of concrete. In: Proceedings of the 5th meeting of the Brazilian Association for Technical Rules, vol 3, pp 126–129
- Cheng AHD (1997) Material coefficients of anisotropic poroelasticity. *International Journal of Rock Mechanics and Mining Sciences* 34(2):199–205
- Chiarelli AS, Shao JF, Hoteit N (2003) Modeling of elastoplastic damage behavior of a claystone. *International Journal of Plasticity* 19:23–45
- Chiu HK, Johnston IW, Donald IB (1983) Appropriate techniques for triaxial testing of saturated soft rock. *International Journal of Rock Mechanics and Mining Sciences* and 20(3):107–120, DOI 10.1016/0148-9062(83)91301-3
- Conil N, Talandier J, Djizanne H, de La Vaissière R, Righini-Waz C, Auvray C, Morlot C, Armand G (2018) How rock samples can be representative of in situ condition: A case study of Callovo-Oxfordian claystones. *Journal of Rock Mechanics and Geotechnical Engineering* 10(4):613–623
- Conil N, Vitel M, Plua C, Vu MN, Seyed D, Armand G (2020) In situ investigation of the thm behavior of the callovo-oxfordian claystone. *Rock Mechanics and Rock Engineering* 53:2747–2769, DOI 10.1007/s00603-020-02073-8
- Coussy O (2004) Poromechanics. J. Wiley & Sons, New York



- Coviello A, Lagioia R, Nova R (2005) On the Measurement of the Tensile Strength of Soft Rocks. *Rock Mechanics and Rock Engineering* 38(4):251–273
- Davy CA, Skoczylas F, Barnichon JD, Lebon P (2007) Permeability of macro-cracked argillite under confinement: Gas and water testing. *Physics and Chemistry of the Earth* 32(8-14):667–680
- Diederichs MS (2007) The 2003 Canadian Geotechnical Colloquium: Mechanistic interpretation and practical application of damage and spalling prediction criteria for deep tunnelling. *Canadian Geotechnical Journal* 44(9):1082–1116
- Donaghe RT, Chaney RC (1988) *Advanced Triaxial Testing of Soil and Rock*, vol 977. ASTM International
- Eberhardt E (2012) The Hoek-Brown failure criterion. *Rock Mechanics and Rock Engineering* 45(6):981–988, DOI 10.1007/s00603-012-0276-4
- Escoffier S (2002) *Caractérisation expérimentale du comportement hydromécanique des argilites de Meuse/Haute-Marne*. PhD thesis, Institut National Polytechnique de Lorraine
- Escoffier S, Homand F, Giraud A, Hoteit N, Su K (2005) Under stress permeability determination of the Meuse / Haute-Marne mudstone. *Engineering Geology* 81(3):329–340
- Ewy RT (2015) Shale/claystone response to air and liquid exposure, and implications for handling, sampling and testing. *International Journal of Rock Mechanics and Mining Sciences* 80:388–401
- Fairhurst C (1961) Laboratory measurement of some physical properties of rock. In: *The 4th US symposium on rock mechanics (USRMS)*, American Rock Mechanics Association, pp 105–118
- Fairhurst C (1964) On the validity of the ‘brazilian’ test for brittle materials. In: *International Journal of Rock Mechanics and Mining Sciences & Geomechanics Abstracts*, Elsevier, vol 1, pp 535–546
- Favero V, Ferrari A, Laloui L (2016) Thermo-mechanical volume change behaviour of Opalinus Clay. *International Journal of Rock Mechanics and Mining Sciences* 90(November 2015):15–25, DOI 10.1016/j.ijrmms.2016.09.013
- Gens A, Vaunat J, Garitte B, Wileveau Y (2007) In situ behaviour of a stiff layered clay subject to thermal loading: observations and interpretation. *Géotechnique* 57(2):207–228
- Ghabezloo S, Sulem J (2009) Stress dependent thermal pressurization of a fluid-saturated rock. *Rock Mechanics and Rock Engineering* 42(1):1–24
- Ghabezloo S, Sulem J (2010) Effect of the volume of the drainage system on the measurement of undrained thermo-poro-elastic parameters. *International Journal of Rock Mechanics and Mining Sciences* 47(1):60–68
- Griffith A (1924) The theory of rupture. In: *Proceedings of the 1st international Congress of applied mechanics*, Tech. Boekhandel en Drukkerij J Walter Jr, Delft, pp 55–63
- Guayacán-Carrillo LM, Ghabezloo S, Sulem J, Seyedi DM, Armand G (2017) Effect of anisotropy and hydro-mechanical couplings on pore pressure evolution during tunnel excavation in low-permeability ground. *International Journal of Rock Mechanics and Mining Sciences* 97:1–14
- Hansen FD, Vogt TJ (1987) Thermo mechanical properties of selected shales. Tech. rep., Oak Ridge National Laboratory Report ORNL/Sub/85-97343/2 (RSI-0305)
- Hawkes I, Mellor M (1970) Uniaxial testing in rock mechanics laboratories. *Engineering Geology* 4:177–285
- Hoek E (1964) Fracture of Anisotropic Rock. *Journal of the South African Institute of Mining and Metallurgy* 64(10):501–518
- Hoek E (1983) Strength of jointed rock masses. *Géotechnique* 33(3):187–223
- Hoek E (2007) *Practical Rock Engineering*. URL <https://www.rocscience.com/assets/resources/learning/\hoek/Practical-Rock-Engineering-Full-Text.pdf>
- Hoek E, Brown E (1980) Empirical strength criterion for rock masses. *Journal of the Geotechnical Engineering Division, ASCE* 106(GT9):1013–1035
- Hoek E, Martin C (2014) Fracture initiation and propagation in intact rock – A review. *Journal of Rock Mechanics and Geotechnical Engineering* 6(4):287–300
- Hoek E, Kaiser PK, Bawden WF (1995) Support of underground excavations in hard rock. January, A.A. Balkma, Rotterdam

- IAPWS-IF97 (2008) IAPWS Industrial Formulation 1997 for the Thermodynamic Properties of Water and Steam. Springer, Berlin, Heidelberg
- ISRM (1978) Suggested Methods for the Quantitative Description of Discontinuities in Rock Masses. *International Journal of Rock Mechanics and Mining Sciences & Geomechanics Abstracts* 15:319–368
- Jobmann M, Polster M (2007) The response of opalinus clay due to heating: A combined analysis of in situ measurements, laboratory investigations and numerical calculations. *Physics and Chemistry of the Earth, Parts A/B/C* 32(8-14):929–936
- Li B, Wong RC (2018) Creating tensile fractures in Colorado shale using an unconfined fast heating test. *Geotechnical Testing Journal* 42(2):296–306
- Mánica MA, Gens A, Vaunat J, Armand G, Vu MN (2021) Numerical simulation of underground excavations in an indurated clay using non-local regularisation. Part 1: formulation and base case. *Géotechnique* pp 1–21, DOI 10.1680/jgeot.20.P.246, URL <https://www.icevirtuallibrary.com/doi/10.1680/jgeot.20.P.246>
- Menaceur H, Delage P, Tang Am, Conil N (2015) The thermo-mechanical behaviour of the Callovo-Oxfordian claystone. *International Journal of Rock Mechanics and Mining Sciences* 78:290–303
- Menaceur H, Delage P, Tang AM, Conil N (2016) On the Thermo-Hydro-Mechanical Behaviour of a Sheared Callovo-Oxfordian Claystone Sample with Respect to the EDZ Behaviour. *Rock Mechanics and Rock Engineering* 49(5):1875–1888
- Mohajerani M, Delage P, Sulem J, Monfared M, Tang AM, Gatmiri B (2012) A laboratory investigation of thermally induced pore pressures in the Callovo-Oxfordian claystone. *International Journal of Rock Mechanics and Mining Sciences* 52:112–121
- Mohajerani M, Delage P, Sulem J, Monfared M, Tang AM, Gatmiri B (2014) The thermal volume changes of the callovo-oxfordian claystone. *Rock Mechanics and Rock Engineering* 47(1):131–142
- Mohamadi M, Wan RG (2016) Strength and post-peak response of Colorado shale at high pressure and temperature. *International Journal of Rock Mechanics and Mining Sciences* 84:34–46
- Monfared M, Delage P, Sulem J, Mohajerani M, Tang AM, De Laure E (2011a) A new hollow cylinder triaxial cell to study the behavior of geo-materials with low permeability. *International Journal of Rock Mechanics and Mining Sciences* 48(4):637–649
- Monfared M, Sulem J, Delage P, Mohajerani M (2011b) A Laboratory Investigation on Thermal Properties of the Opalinus Claystone. *Rock Mechanics and Rock Engineering* 44(6):735–747
- Palciauskas VV, Domenico PA (1982) Characterization of drained and undrained response of thermally loaded repository rocks. *Water Resources Research* 18(2):281–290
- Pardoën B, Seyedi DM, Collin F (2015) Shear banding modelling in cross-anisotropic rocks. *International Journal of Solids and Structures* 72:63–87, DOI 10.1016/j.ijsolstr.2015.07.012, URL <http://dx.doi.org/10.1016/j.ijsolstr.2015.07.012>
- Perras MA, Diederichs MS (2014) A Review of the Tensile Strength of Rock: Concepts and Testing. *Geotechnical and Geological Engineering* 32(2):525–546, DOI 10.1007/s10706-014-9732-0
- Pham QT, Vales F, Malinsky L, Minh DN, Gharbi H (2007) Effects of desaturation – resaturation on mudstone. *Physics and Chemistry of the Earth* 32:646–655
- Plúa C, Vu MN, Armand G, Rutqvist J, Birkholzer J, Xu H, Guo R, Thatcher KE, Bond AE, Wang W, Nagel T, Shao H, Kolditz O (2021a) A reliable numerical analysis for large-scale modelling of a high-level radioactive waste repository in the Callovo-Oxfordian claystone. *International Journal of Rock Mechanics and Mining Sciences* 140(February), DOI 10.1016/j.ijrmms.2020.104574
- Plúa C, Vu MN, Seyedi DM, Armand G (2021b) Effects of inherent spatial variability of rock properties on the thermo-hydro-mechanical responses of a high-level radioactive waste repository. *International Journal of Rock Mechanics and Mining Sciences* 145(February):104682, DOI 10.1016/j.ijrmms.2021.104682, URL <https://doi.org/10.1016/j.ijrmms.2021.104682>
- Robinet JC, Sardini P, Coelho D, Parneix JC, Prt D, Sammartino S, Boller E, Altmann S (2012) Effects of mineral distribution at mesoscopic scale on solute diffusion in a clay-rich rock: Example of the Callovo-Oxfordian mudstone (Bure, France). *Water Resources Research* 48(5), DOI 10.1029/2011WR011352

- Seyedi D, Armand G, Conil N, Vitel M, Vu MN (2017) On the Thermo-Hydro-Mechanical Pressurization in Callovo-Oxfordian Claystone under Thermal Loading. In: *Poromechanics 2017 - Proceedings of the 6th Biot Conference on Poromechanics*, pp 754–761
- Sultan N, Delage P, Cui Y (2002) Temperature effects on the volume change behaviour of boom clay. *Engineering Geology* 64(2-3):135–145
- Tourchi S, Vaunat J, Gens A, Bumbieler F, Vu MN, Armand G (2021) A full-scale in situ heating test in Callovo-Oxfordian claystone: observations, analysis and interpretation. *Computers and Geotechnics* 133(February), DOI 10.1016/j.compgeo.2021.104045
- Valès F, Nguyen Minh D, Gharbi H, Rejeb A (2004) Experimental study of the influence of the degree of saturation on physical and mechanical properties in Tournemire shale (France). *Applied Clay Science* 26:197–207, DOI 10.1016/j.clay.2003.12.032
- Vu MN, Armand G, Plua C (2020) Thermal Pressurization Coefficient of Anisotropic Elastic Porous Media. *Rock Mechanics and Rock Engineering* 53(4):2027–2031, DOI 10.1007/s00603-019-02021-1, URL <https://doi.org/10.1007/s00603-019-02021-1>
- Wild KM, Walter P, Amann F (2017) The response of Opalinus Clay when exposed to cyclic relative humidity variations. *Solid Earth* 8(2):351–360, DOI 10.5194/se-8-351-2017
- Wileveau Y, Cornet FH, Desroches J, Blumling P (2007) Complete in situ stress determination in an argillite sedimentary formation. *Physics and Chemistry of the Earth* 32(8-14):866–878
- Yang MT, Hsieh HY (1997) Direct tensile behavior of a transversely isotropic rock. *International Journal of Rock Mechanics and Mining Sciences* 34(5):837–849
- Zhang C, Rothfuchs T (2004) Experimental study of the hydro-mechanical behaviour of the Callovo-Oxfordian argillite. *Applied Clay Science* 26(1-4):325–336, DOI 10.1016/j.clay.2003.12.025
- Zhang CL, Conil N, Armand G (2017) Thermal effects on clay rocks for deep disposal of high-level radioactive waste. *Journal of Rock Mechanics and Geotechnical Engineering* 9(3):463–478
- Zhang F, Xie SY, Hu DW, Shao JF, Gatmiri B (2012) Effect of water content and structural anisotropy on mechanical property of claystone. *Applied Clay Science* 69:79–86